

Thermomechanical–microstructural modelling of nodular cast iron solidification

D. J. Celentano*¹, P. M. Dardati², F. D. Carazo² and L. A. Godoy³

This paper presents a thermomechanical–microstructural formulation for the analysis of the solidification process of nodular cast irons of eutectic composition. This formulation is defined in a finite strain thermoplasticity framework considering multinodular microstructure based liquid–solid phase change effects. The performance of this model is evaluated in the analysis of a solidification test for which some laboratory measurements are available. Computed temperature and displacement evolutions together with final values of austenite and graphite volumetric fractions and density of graphite nodules are all found to reasonably agree with the corresponding experimental measurements. This analysis illustrates the possibility of tackling different coupled and complex phenomena occurring in casting problems.

Keywords: Ductile iron, Solidification, Microstructure, Modelling

Introduction

The study of the nodular [also called ductile or spheroidal graphite (SG)] cast iron solidification and the subsequent cooling processes is still nowadays an active research area, mainly due to the different and complex phenomena involved in the analysis. The industrial relevance of SG cast iron is due to its advantageous mechanical properties that make it as an attractive option to replace traditional cast or forged steels in many engineering applications. Among the several factors that directly affect the final soundness of the castings, it is possible to identify the microstructure evolution and characterisation,^{1,2} the presence of residual stresses, the geometrical changes caused by thermal contraction and metallurgical transformations and the influence of heat treatments and phase contents on the mechanical properties.^{3–5}

The mechanical properties of SG cast iron parts have been long recognised to strongly depend on the chemical composition of the different alloying elements and on the final microstructure.⁶ In particular, the influences of the graphite nodule shapes on the wear and fatigue characteristics of cast iron have been also investigated where a considerable increase in wear loss was found for a decrease in graphite nodularity and, in addition, when changing graphite shape from spheroidal to flake.⁷ Experimental results related to the characterisation of the graphite morphology showed that size, shape and distribution of the graphite nodules have no significant

influence on cyclic hardening of the material, but they play a great role in the crack initiation and propagation process such that the larger irregularly shaped nodules reduce fracture toughness and fatigue strength.⁸

In the modelling of SG cast iron solidification, relevant efforts have been made to couple heat flow calculations performed at the macroscopic level to related microscopic phenomena such as phase appearance, morphology and grain size of the solidified product (*see*, e.g. Ref. 9 for a recent review on this subject). At present, there are two main theories to explain the solidification behaviour of SG cast iron. In the uninodular theory, the growth of graphite nodules occurs by carbon depositing directly from the liquid or by diffusion through a layer of solid austenite that surrounds a nodule (both graphite and austenite having spherical shape) or by a combination of both mechanisms (*see*, e.g. Zhao and Liu¹⁰). In the multinodular theory, on the contrary, the austenite nucleates independently and grows in dendritic form while graphite grows with spherical shape: initially, graphite grows in contact with liquid, but as it gains contact with austenite, then the spherical nodules are surrounded by austenite; once graphite is wrapped by austenite, the graphite spheres grow by diffusion of carbon, from the liquid, through the austenite (*see*, e.g. Boeri and Sikora¹¹). More sophisticated simulations employing the multinodular approach have been developed afterwards. In particular, Dardati *et al.*¹² proposed a thermal–microstructural formulation for the simulation of equiaxial solidification of eutectic SG cast iron according to multinodular assumptions. This analysis included the spherical nodules of graphite as well as the dendritic growth of austenite, and, in addition, the mass balance of solute (carbon) satisfied at all instants of the process. This model allows obtaining microstructural features arising from the solidification process, such as the density and distribution of the size of graphite nodules, grain size of austenite and patterns of microsegregation. A good quantitative agreement between experimental and

¹Departamento de Ingeniería Mecánica y Metalúrgica, Pontificia Universidad Católica de Chile, Av. Vicuña Mackenna 4860, Santiago, Chile

²Departamento de Ingeniería Mecánica y CIII, Facultad Regional Córdoba, UTN, Maestro M. López esq. Cruz Roja Argentina s/n, Ciudad Universitaria, Córdoba, Argentina

³Departamento Estructuras, FCEfYN, Universidad Nacional de Córdoba y CONICET, Av. Vélez Sarsfield 1601, Córdoba, Argentina

*Corresponding author, email dcelentano@ing.puc.cl

computational cooling curves was found. A further experimental validation of the numerical results provided by this model was presented in Celentano *et al.*¹³ together with a sensitivity analysis of the response with respect to changes in the cooling rate and nucleation parameters. Moreover, an experimental and a numerical study of the solidification process of ductile cast iron under slightly hypereutectic conditions in tests performed using standardised cups has been reported in Dardati *et al.*¹⁴ The experimental tasks involved recording of cooling curves at the centre of the cup and metallographic studies to investigate the number and size of graphite nodules at the end of the process. Different models were tested: a model based on a uninodular theory and two models that represent the multinodular theory. These three models were found to provide very similar temperature evolutions and final graphite density nodule distributions. Although the computed cooling curves were in good agreement with the experimental measurements, some scatter was found, however, in the numerical–experimental comparison for the graphite nodule density at different points of the sample. More recently, a two-dimensional model for simulating the ductile iron structure formation during solidification has been developed by Burbelko *et al.*¹⁵ This model, solved with a cellular automaton finite difference technique, takes into account the continuous nucleation of austenite and graphite grains from liquid, separate growth of graphite nodules and austenite dendrites at the first solidification stage and the following cooperative growth of graphite–austenite eutectic in the binary Fe–C system. Furthermore, Zhao and Liu¹⁶ established and applied to a practical industrial component a model for microstructure formation, feeding flow calculation and porosity prediction during the solidification and cooling processes of SG cast iron. The porosity values obtained with this model were numerically assessed, while the computed ferrite and pearlite fractions were experimentally validated.

On the other hand, several thermomechanical models, aimed at predicting thermal residual stresses and final shapes in SG cast iron parts in order to prevent macroscopic defects and/or to optimise operational conditions, have been developed during the last two decades. More recently, Celentano¹⁷ considered various microstructural aspects in thermomechanical simulations of solidification and cooling processes of SG cast iron where simple microscopic models of microstructure formation (i.e. nucleation and growth laws based only on the local undercooling) were coupled to macroscopic thermomechanical computations to assess the influence of the evolution of both micro- and macrofeatures on the full response of the materials involved in the casting system. In this last context, in sharp contrast to purely thermomechanical models, phase change effects are assumed to depend not only on temperature but also on temperature rate by means of other appropriate microscopic variables to simulate in a more realistic form the complex phenomena associated with the phase transformation. However, it should be noted that this phenomenological approach includes the definition of evolution laws for the phase change variables assumed to govern the average microstructure formation occurring in a certain (preferably small) volume at the macroscopic level and, hence, precludes a microscopic scale modelling of the micromechanisms developed

during the process, which, with the present computer power, is in most cases an impossible task.

This work presents a new thermomechanical–microstructural formulation for the analysis of the solidification process of SG cast irons with eutectic composition. This formulation, defined within the thermoplasticity context, includes large strain effects, phase change volumetric deformations, temperature dependent material properties and microstructure evolution governed by a multinodular based eutectic solidification model. This macro–microapproach, which constitutes the principal original contribution of this work, is intended to provide a more realistic description of the material response during solidification with the final aim to achieve a better control of the material properties of the parts obtained through this industrially relevant process. The thermomechanical formulation is presented in the section on ‘Thermomechanical formulation’. The section on ‘Elastoplastic constitutive model’ includes the elastoplastic constitutive model assumed to describe the behaviour of all the materials involved in the casting system and, in particular, the liquid, mushy and solid phases that take place during the solidification and cooling of the alloy. Furthermore, the liquid–solid phase change described by a microstructure model of the eutectic SG cast iron is detailed in the section on ‘Microstructural model’. The microstructure mechanisms encompass kinetic based nucleation and growth laws for both the dendritic austenite and graphite nodules. On the other hand, the solid–solid (eutectoid) phase change is simply considered via a macroscopic (i.e. only temperature dependent) model. This thermomechanical–microstructural model is discretised and solved in the context of the finite element method. Finally, the analysis of a solidification test is performed in the section on ‘Solidification test’ with the aim of comparing some available experimental measurements with the numerical results obtained using this proposed formulation.

Thermomechanical formulation

The fully coupled (i.e. bidirectional) thermomechanical formulation used in the present work is based on that proposed in Refs. 17 and 18. Therefore, only the main features of it are described below.

In a general thermomechanical context, the local governing equations describing the evolution of a process can be expressed by the continuity equation, the equation of motion, the energy balance and the dissipation inequality (all of them valid in $\Omega \times Y$, where Ω is the spatial configuration of a body and Y denotes the time interval of interest, with $t \in Y$) respectively written in a Lagrangian description as

$$\rho J = \rho_0 \tag{1}$$

$$\nabla \sigma + \rho \mathbf{b}_f = \rho \ddot{\mathbf{u}} \tag{2}$$

$$-\rho c \dot{T} - \nabla \mathbf{q} + \rho r - T \boldsymbol{\beta} : \mathbf{d} + \rho r_{\text{int}} = 0 \tag{3}$$

together with appropriate boundary and initial conditions and adequate constitutive relations for the Cauchy stress tensor σ (which is symmetric for the non-polar case adopted in the present work), the tangent specific heat capacity c , the heat flux vector \mathbf{q} , the tangent conjugate of the thermal dilatation tensor $\boldsymbol{\beta}$ and the

specific internal heat source r_{int} . In these equations, ∇ is the spatial gradient operator, the superposed dot indicates time derivative, and the subscript 0 applied to a variable denotes its value at the initial configuration Ω_0 . Moreover, ρ is the density, \mathbf{u} is the displacement vector, J is the determinant of the deformation gradient tensor \mathbf{F} ($\mathbf{F}^{-1} = \mathbf{1} - \nabla \times \mathbf{u}$, with $\mathbf{1}$ being the unity tensor), \mathbf{b}_f is the specific body force vector, T is the temperature, r is the specific heat source and \mathbf{d} is the rate of deformation tensor ($\mathbf{d} = 1/2(\nabla \times \mathbf{v} + \mathbf{v} \times \nabla)$, where $\mathbf{v} = \dot{\mathbf{u}}$ is the velocity vector). In this framework, a specific Helmholtz free energy function ψ , assumed to describe the material behaviour during the thermomechanical process, can be defined in terms of some thermodynamic state variables chosen in the present work as the Almansi strain tensor \mathbf{e} ($\mathbf{e} = 1/2(\mathbf{1} - \mathbf{F}^{-1}\mathbf{F}^{-1})$, where T is the transpose symbol), the temperature and a set of n_{int} phenomenological internal variables α_k (usually governed by rate equations with $k = 1, \dots, n_{int}$) accounting for the non-reversible effects. This free energy definition is only valid for small elastic strains and isotropic material response, both assumptions being normally accepted for metals and other materials. Invoking the Coleman's method, the following relationships are obtained: $\boldsymbol{\sigma} = \rho(\partial\psi/\partial\mathbf{e})$, $c = -T(\partial^2\psi/\partial T^2)$, $\boldsymbol{\beta} = -\rho(\partial^2\psi/\partial\mathbf{e}\partial T) = -(\partial\boldsymbol{\sigma}/\partial T)$ and $r_{int} = -(1/\rho)[T(\partial\mathbf{q}_k/\partial T) - \mathbf{q}_k]^*(D\alpha_k/Dt)$ where $\mathbf{q}_k = -\rho(\partial\psi/\partial\alpha_k)$ are the conjugate variables of α_k , and, according to the nature of each internal variable, the symbols * and $D(\cdot)/Dt$ appearing in the previous expressions respectively indicate an appropriate multiplication and a time derivative satisfying the principle of material frame indifference. Furthermore, the heat flux vector at the spatial configuration is assumed to be given by the Fourier's law written as $\mathbf{q} = -k\nabla T$, where k is the conductivity coefficient.

It is seen that the definitions of $\psi = \psi(\mathbf{e}, \alpha_k, T)$ and $D\alpha_k/Dt$ are crucial features of the formulation in order to derive the constitutive equations presented above. To this end, the following split is adopted: $n_{int} = n_{int}^p + n_{int}^{pc}$, where n_{int}^p and n_{int}^{pc} refer to the number of internal variables related to plastic (non-reversible that may occur in every material of the casting system) and phase change (only existing in the solidifying alloy) effects respectively. Accordingly, this assumption leads to $r_{int} = r_{int}^p + r_{int}^{pc}$. Details of the elastoplastic and micro-structure models are given below.

Elastoplastic constitutive model

In this present work, the material behaviour in the mushy zone is assumed to be governed by a mixed rule that weights the responses of the liquid l and solid s phases according to their respective volumetric fractions f . Thus, any mixed variable can be defined as

$$\chi|_{mx} = \sum_{cp=1,s} f_{cp}\chi|_{cp} = f_l\chi|_l + f_s\chi|_s \quad (4)$$

such that $\sum_{cp=1,s} f_{cp} = f_l + f_s = 1$.

The internal variables and their corresponding evolution equations are defined in the present work within the associate rate independent thermoplasticity theory context. This framework has been chosen for the constitutive description of the whole casting system since little rate sensitiveness is expected in the material response due to the rapid evolution of the solidification and

cooling processes. Moreover, this assumption is additionally supported by the fact that very similar thermo-mechanical behaviours have been obtained using plastic and viscoplastic (with a relatively large range of viscosity values) models in the numerical simulation of casting problems (see Ref. 17).

A possible choice for the internal variables is given by the plastic Almansi strain tensor \mathbf{e}^p and the effective plastic deformation \bar{e}^p related to the isotropic strain hardening effect (i.e. $n_{int}^p = 2$ with $\alpha_1 = \mathbf{e}^p$ and $\alpha_2 = \bar{e}^p$). The evolution equations for such plastic variables are written as

$$L_v(\mathbf{e}^p) = \dot{\lambda}(\partial F/\partial\boldsymbol{\sigma}) \quad \dot{\bar{e}}^p = -\dot{\lambda}(\partial F/\partial C) \quad (5)$$

where L_v is the well known Lie (frame indifferent) derivative, $\dot{\lambda}$ is the plastic consistency parameter computed according to classical concepts of the plasticity theory, C is the plastic isotropic hardening function and $F = F(\boldsymbol{\sigma}, \bar{e}^p, T)$ is the yield function governing the plastic behaviour of the solid such that no plastic evolutions occur when $F < 0$. A von Mises yield function is adopted

$$F = (3J_2)^{1/2} - C_y|_{mx} \quad (6)$$

where J_2 is the second invariant of the deviatoric part of $\boldsymbol{\sigma}$ [$\sigma_{eq} = (3J_2)^{1/2}$ is the so called equivalent or von Mises stress], and the yield strength function $C_y|_{cp}$ is adopted in the present work as

$$C_y|_{cp} = C_{y0}|_{cp} + C \quad (7)$$

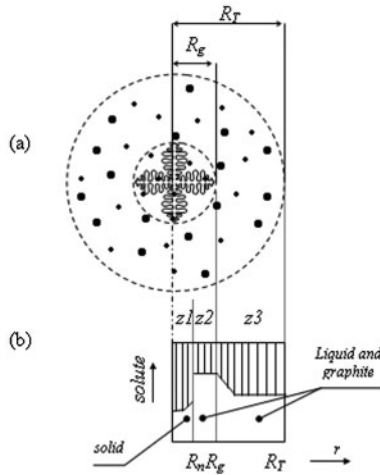
with $C_{y0}|_{cp} = C_{y0}|_{cp}(T)$ being the yield strength defining the initial material elastic bound. In general, $C_{y0}|_{cp}$ decreases with temperature, and hence, it accounts for the thermal softening phenomenon, which is an important effect to be considered in casting processes where materials undergoing large temperature variations are involved. For the liquid phase, in particular, $C_{y0}|_l = 0$ is assumed.

Assuming a stress free initial state ($\boldsymbol{\sigma}_0 = \mathbf{0}$), the following specific free energy function $\psi = \psi|_{mx}$ is proposed such that $\psi|_{cp} = \psi|_{cp}(\mathbf{e} - \mathbf{e}^p, \bar{e}^p, T)$ is expressed as

$$\begin{aligned} \psi|_{cp} = & \frac{1}{2\rho}(\mathbf{e} - \mathbf{e}^p - \mathbf{e}^{th}|_{cp} - \mathbf{e}^{pc}) : \mathbf{C}^s|_{cp} : (\mathbf{e} - \mathbf{e}^p - \mathbf{e}^{th}|_{cp} - \mathbf{e}^{pc}) + \\ & \frac{1}{(n^p|_{cp} + 1)\rho} A^p|_{cp} \bar{e}^{n^p|_{cp} + 1} + c^s|_{cp} [(T - T_0) - T \ln(T/T_0)] + \\ & \psi_L - \eta_0(T - T_0) + \psi_0|_{cp} \end{aligned} \quad (8)$$

where $\mathbf{C}^s|_{cp}$ is the secant isotropic elastic constitutive tensor, $A^p|_{cp}$ and $n^p|_{cp}$ are the parameters aimed at characterising the isotropic hardening behaviour of the material, $c^s|_{cp}$ is the secant specific heat and ψ_L is the term that includes the latent heat effects. It should be noted that the deviatoric response of the liquid phase is neglected by assuming a purely volumetric elastic constitutive tensor in this phase. Furthermore, $\mathbf{e}^{th}|_{cp}$ and \mathbf{e}^{pc} are the thermal and phase change Almansi strain tensors respectively given by

$$\mathbf{e}^{th}|_{cp} = \frac{1}{2} \left[1 - (1 - a_{th}|_{cp})^{2/3} \right] \mathbf{1} \quad (9)$$



1 a schematic representation of equiaxial dendrite grain and spherical graphite nodules and b spherical solute concentration (spherical symmetry is assumed)

$$e^{pc} = \frac{1}{2} \left[1 - (1 - a_{pc})^{2/3} \right] \left(1 - a_{th|cp} \right)^{2/3} \quad (10)$$

where $a_{th|cp} = \alpha_{th|cp}^s (T - T_{ref}) - \alpha_{th0|cp}^s (T_0 - T_{ref})$ with $\alpha_{th|cp}^s$ being the secant volumetric thermal dilatation coefficient and $a_{pc} = \delta_{pc}^s|_s f_s + \delta_{pc}^s|_e f_e$ where $\delta_{pc}^s|_{ph}$ ($ph=s,e$) are the secant volumetric deformations respectively related to the liquid–solid and solid–solid phase changes, and f_e is the eutectoid volumetric fraction accounting for the solid–solid phase change. Moreover, $\psi_L = L^s|_s f_s + L^s|_e f_e$ such that $L^s|_{ph}$ ($ph=s,e$) are the respective secant specific latent heats. In the present work, f_s is computed according to the microstructure model presented below, while f_e is assumed to be simply given by a linear relationship defined in terms of two temperatures associated with the beginning and end of the eutectoid transformation.

As mentioned above, the proposed definition of ψ allows the derivation, including coupled thermoelastic, thermoplastic and phase change effects, of all the constitutive equations given in the section on ‘Thermomechanical formulation’.

Microstructural model

The eutectic SG cast iron microstructure solidification model adopted in the present work corresponds to that proposed in Ref. 12. In this model, the phase change internal variables are the austenite and graphite volumetric fractions together with their respective grain/nodule density and radius (i.e. $n_{int}^{pc}=6$). Only a brief description of this model is presented below.

Solid fraction

Figure 1a shows a schematic representation of an equiaxial dendrite grain and spherical graphite nodules. The total grain radius R_T is computed at the instant of instantaneous nucleation. The radius R_g corresponds to a spherical surface at the tip of the main dendrites and grows during the solidification until it reaches the value R_T . Three spherical symmetric zones are identified in Fig. 1b in order to produce a simplified description of the solute concentration. Zone z1, defined as a sphere

with radius R_n with variable solute content, covers the volumetric fraction corresponding to the total solid volume of the grain. Zone z2 presents a uniform distribution of solute in the interdendritic liquid, while zone z3 exhibits a variation of solute concentration in the intergranular region. In this context, the solid fraction is written as

$$f_s = f_\gamma + f_{gr} \quad (11)$$

where f_γ and f_{gr} are the austenite and graphite volumetric fraction respectively given by

$$f_\gamma = \left(\frac{R_n}{R_T} \right)^3 - f_{gr}^{Z_1} \quad (12)$$

$$f_{gr} = \sum_{i=1}^3 f_{gr}^{Z_i} \quad (13)$$

such that the graphite volumetric fraction of graphite associated to zone z_i ($i=1, 2, 3$) is

$$f_{gr}^{Z_i} = \frac{4}{3} \pi \sum_{j=1}^k N_{gr_j}^{Z_i} R_{gr_j}^{Z_i 3} \quad (14)$$

where $N_{gr_j}^{Z_i}$ is the number of graphite nodules per unit volume of total grain of zone z_i with radius $R_{gr_j}^{Z_i}$, the subscript j denotes the nodule group related to a specific nucleation time, and k stands for the total number of nodule groups.

Nucleation and growth of austenite

Nucleation of the austenite is assumed to occur as soon as the eutectic temperature T_E is reached. The following instantaneous nucleation law is adopted

$$N_\gamma = A_\gamma \dot{T} \quad (15)$$

where N_γ is the density of austenite grains, and A_γ is a parameter that depends on the characteristics of liquid such as composition, superheating and holding time.

Based on the number of austenite grains that nucleate per unit volume, the total radius R_T is simply computed as

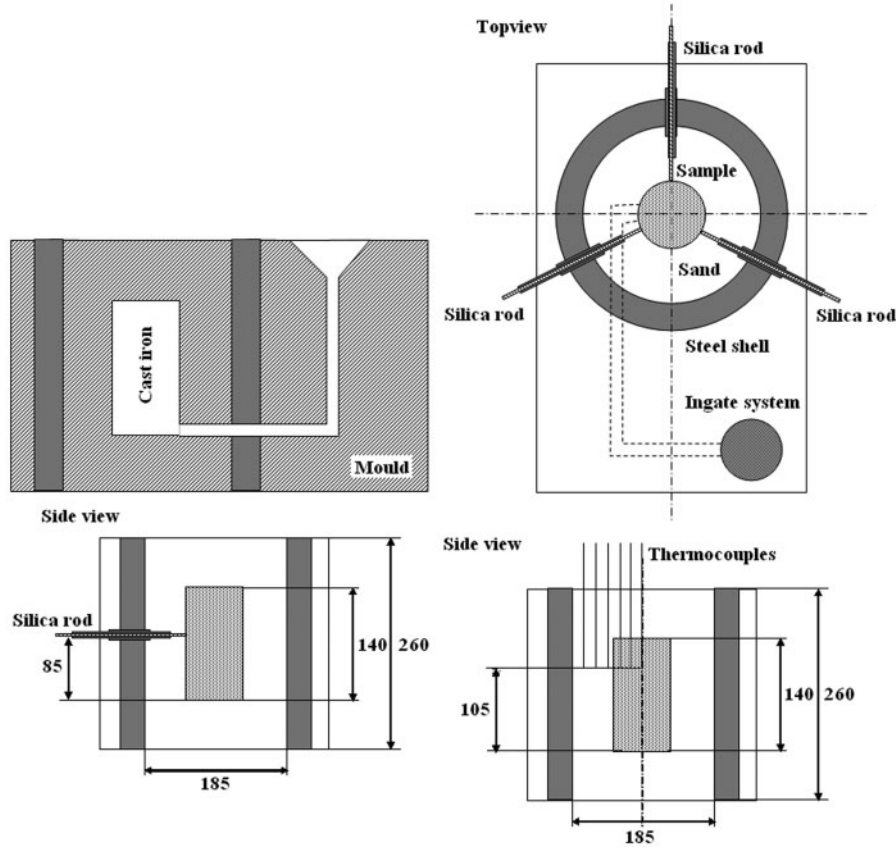
$$R_T = \left(\frac{3}{4\pi N_\gamma} \right)^{1/3} \quad (16)$$

The growth of the dendrite tips is assumed to be controlled by the diffusion of solute, while the influence of the thermal undercooling is neglected because the temperature is considered as constant for the whole grain. The evolution of R_g is given by

$$\dot{R}_g = \frac{D_c^l m C_0}{\pi^2 \Gamma (k_p - 1)} \left(\frac{C^{l/\gamma} - C_\infty}{C_0} \right)^2 \quad (17)$$

where D_c^l is the coefficient of carbon diffusion in liquid, m is the slope of the austenite liquidus curve, C_0 is the initial concentration of carbon, γ is the Gibbs–Thompson coefficient, k_p is the partition coefficient, $C^{l/\gamma}$ is the carbon concentration of the liquid in contact with austenite (at equilibrium for a given temperature T) and C_∞ is the carbon concentration of the intergranular liquid away from the dendrite tip.

Moreover, the radius evolution of the spherical zone z1 is evaluated by equating its volume to the sum of the



2 Experimental apparatus

eutectic austenite volume plus the volume of nodules that have already been surrounded by this phase and that do not continue growing according to this model. Thus

$$\dot{R}_n = \frac{3 R_g^2 (C^{1/\gamma} - C_\infty) \dot{R}_g + (R_g^3 - R_n^3) \dot{C}^{1/\gamma}}{3 C^{1/\gamma} (1 - k_p) R_n^2} \quad (18)$$

Nucleation and growth of graphite

Graphite nucleation is modelled as a continuous process that occurs in zones z2 and z3 according to the following law

$$\dot{N}_{gr}^{z_i} = b_{gr} \Delta T \exp\left(-\frac{c_{gr}}{\Delta T}\right) (1 - f_s^{z_i}) \quad (19)$$

where b_{gr} and c_{gr} are nucleation parameters that depend on the composition and liquid treatment, and ΔT is the undercooling.

Graphite nodules grow in both the interdendritic and intergranular liquids, but with different rates because zones z2 and z3 have different carbon concentrations, named $C^{1/\gamma}$ and C_∞ respectively. The growth of graphite nodules due to diffusion is modelled here using Zener’s equation for a spherical isolated particle in a matrix with low saturation

$$\dot{R}_{grj}^{z_2} = \frac{D_c^l \rho_l (C^{1/\gamma} - C^{l/gr})}{R_{grj} \rho_{gr} (C_{gr} - C^{l/gr})} \quad \dot{R}_{grj}^{z_3} = \frac{D_c^l \rho_l (C_\infty - C^{l/gr})}{R_{grj} \rho_{gr} (C_{gr} - C^{l/gr})} \quad (20)$$

where $C^{l/gr}$ is the carbon concentration of the liquid in contact with graphite (at equilibrium for a given

temperature T), and C_{gr} is the carbon concentration of graphite (i.e. 100%).

The thermomechanical–microstructural model presented above is discretised and solved in the context of the finite element method (see Ref. 17 for further details).

Solidification test

The analysis of a cylindrical casting specimen of SG cast iron (diameter=70 mm and height=140 mm) in a green sand mould surrounded by a steel shell (internal diameter=185 mm, thickness=30 mm and height=260 mm) is performed. The experimental apparatus is schematically shown in Fig. 2. This test, preliminarily reported in Ref. 17, has been carried out again in order to obtain more accurate and repeatable experimental measurements, which are used in the present work for validation purposes of the thermomechanical–microstructural formulation presented in the sections on ‘Thermomechanical formulation’, ‘Elastoplastic constitutive model’ and ‘Microstructural model’. Both temperature and radial displacement evolutions have been measured during solidification and cooling approximately at the midheight of the specimen. Thermocouples were placed on three radial directions at 0, 120 and 240°, starting from the cylinder central axis to the surrounding sand mould in order to visualise the thermal gradient evolution. Radial displacements were measured at the same directions on the cylinder external skin using silica rods. Both temperature and displacement measurements correspond to average values where the maximum standard deviation were 5°C for the temperature measurements within the liquid–solid and solid–solid phase change intervals (it increased, however, to 15°C

outside these ranges) and 0.2 mm for the radial displacement measurements. In addition, microstructural analysis via metallography has been carried out to obtain the number and size of graphite nodules at the end of the process.

The material thermomechanical properties for the SG cast iron, green sand and steel are respectively summarised in Tables 1–3.^{12,14,17,19} The heat transfer coefficients of the different interfaces are shown in Table 4.¹⁷

The axisymmetric numerical computation used 540 four-noded isoparametric elements and a time step of 1.5 s. The analysis starts with the mould cavity completely filled with molten metal at rest at 1250°C (i.e. instantaneous filling is assumed) and 22°C for the sand and steel moulds. The mould is simply supported at the bottom, and convection–radiation conditions have been considered between the external face of the mould and the environment. Mechanical frictionless contact conditions are adopted for the casting/sand interface.

The experimental temperature evolutions in the casting and mould for different radial positions at height 105 mm are plotted in Fig. 3. The numerical results obtained with the proposed formulation are also included for comparison. A good overall agreement can be observed where, more specifically, the liquid–solid

and solid–solid phase changes are reasonably well described.

The experimental and numerical radial displacement evolutions at height 85 mm of the casting/mould interface are shown in Fig. 4. The different expansion/contraction behaviours related to the phase changes occurring during the process can clearly be seen:

- (i) contraction until the beginning of the solidification
- (ii) expansion during solidification (graphite precipitation)
- (iii) contraction from the end of the solidification up to the beginning of the eutectoid transformation
- (iv) expansion during the eutectoid transformation
- (v) final contraction to room temperature.

Almost identical behaviours have been experimentally observed for the three directions mentioned above, and therefore, an average curve has been included in Fig. 4. The response provided by the SG model proposed in the present work correctly reproduces the distinct behaviours observed at those different stages of the process (it should be noted that the displacement evolutions computed in the present work are quantitatively more realistic than those reported in Ref. 17). Moreover, Fig. 5 depicts the deformed configurations at four times of the analysis. It is seen that the differential vertical

Table 1 Thermomechanical–microstructural properties of nodular cast iron^{12,14,17}

Temperature/°C	Young's modulus/MPa	Thermal dilatation/°C ⁻¹	Yield strength/MPa
20	163 500	13 × 10 ⁻⁶	260
100	163 100	13 × 10 ⁻⁶	255
200	160 200	13 × 10 ⁻⁶	250
300	151 600	13 × 10 ⁻⁶	230
400	135 300	13 × 10 ⁻⁶	210
500	110 900	13 × 10 ⁻⁶	130
600	81 400	13 × 10 ⁻⁶	60
700	52 000	13 × 10 ⁻⁶	50
720	46 700	13 × 10 ⁻⁶	48
750	44 300	12 × 10 ⁻⁶	45
770	43 800	12 × 10 ⁻⁶	42
800	44 400	12 × 10 ⁻⁶	40
900	35 400	15 × 10 ⁻⁶	30
1000	28 400	17 × 10 ⁻⁶	20
1100	5000	18 × 10 ⁻⁶	10
1150	10	20 × 10 ⁻⁶	2
1400	10	20 × 10 ⁻⁶	0

Poisson's ratio: 0.33

Hardening parameters: $A^p=300$ MPa; $n^p=0.22$

Phase change volumetric deformation: 0.01 (eutectic), 0.005 (eutectoid)

Temperature/°C	Conductivity/W m ⁻¹ °C ⁻¹	Specific heat/J kg ⁻¹ °C ⁻¹
20	44.1	500
280	44.1	600
420	40.9	700
560	37.1	750
700	33.6	750
840	28.1	750
980	22.5	820
1120	18.8	840
1250	120.0	840
1400	120.0	840

Density/kg m⁻³: 7000

Latent heat/kJ kg⁻¹: 230 (eutectic), 84 (eutectoid)

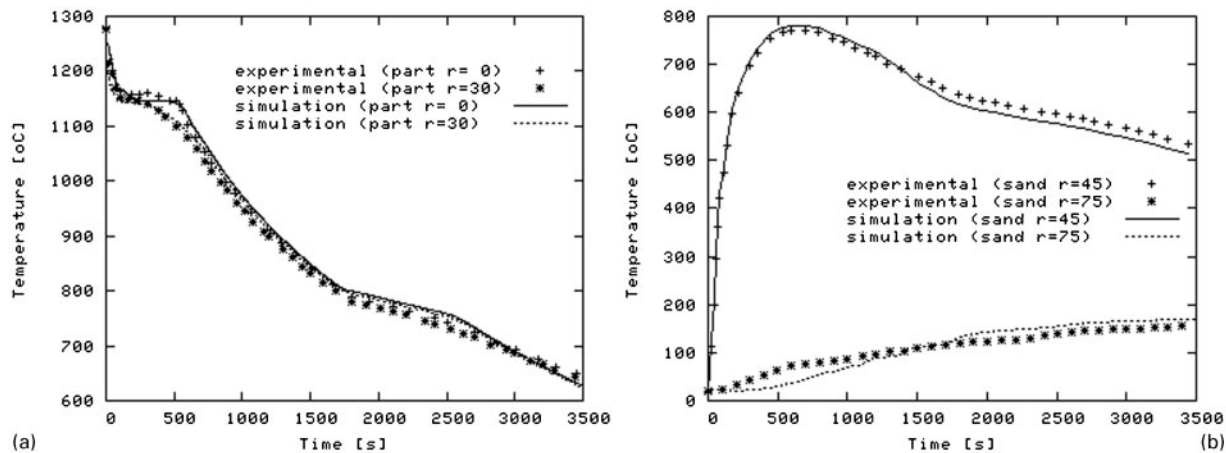
Carbon diffusion coefficient/m² s⁻¹: $D_c^l=5.0 \times 10^{-10}$

Graphite nucleation parameters: $b_{gr}=4.0 \times 10^{13}$ nuclei m⁻³ °C⁻¹ s⁻¹, $c_{gr}=340$ °C

Austenite nucleation parameter (nuclei/s m⁻³ °C⁻¹): $A_\gamma=1.0 \times 10^7$

Gibbs–Thompson coefficient/°K m⁻¹: 2.0×10^{-7}

Initial concentrations: $C_0=3.5$ and $Si_0=2.0$



3 Experimental and computed temperature evolutions in a casting and b mould for different radial positions at height 105 mm of specimen

dilatation between the casting and sand mould that develops during the cooling process makes the measurement tasks difficult since the silica rods can be potentially broken as a consequence of the action of an unacceptable shear force.

The volumetric fractions evolutions in the casting for two radial distances at height 105 mm of the specimen are plotted in Fig. 6. The final values of these fractions were found to be consistent with the metallographic observations (i.e. 0.92 ± 0.2 and 0.08 ± 0.1 for the

Table 2 Thermomechanical properties of green sand^{17,19}

Young's modulus/MPa: 150

Poisson's ratio: 0.33

Thermal dilatation/ $^{\circ}\text{C}^{-1}$: 13×10^{-6}

Yield strength/MPa: 5 (perfect plasticity is assumed)

Phase change volumetric deformation: 0.01 (due to water evaporation)

Temperature/ $^{\circ}\text{C}$	Conductivity/ $\text{W m}^{-1} \text{ }^{\circ}\text{C}^{-1}$	Specific heat/ $\text{J kg}^{-1} \text{ }^{\circ}\text{C}^{-1}$
100	0.478	1045
200	0.505	1071
300	0.505	1096
400	0.516	1120
500	0.511	1143
600	0.507	1167
700	0.507	1191
800	0.517	1215
900	0.547	1238
1000	0.600	1262
1100	0.682	1285
1200	0.805	1309
1300	0.973	1333
1400	1.194	1356

Density/ kg m^{-3} : 1530

Latent heat/ kJ kg^{-1} : 3.75 (initial free water volumetric fraction: 0.047)

Table 3 Thermomechanical properties of steel¹⁷

Young's modulus/MPa: 210 000

Poisson's ratio: 0.3

Thermal dilatation/ $^{\circ}\text{C}^{-1}$: 12×10^{-6}

Yield strength/MPa: 210 (perfect plasticity is assumed)

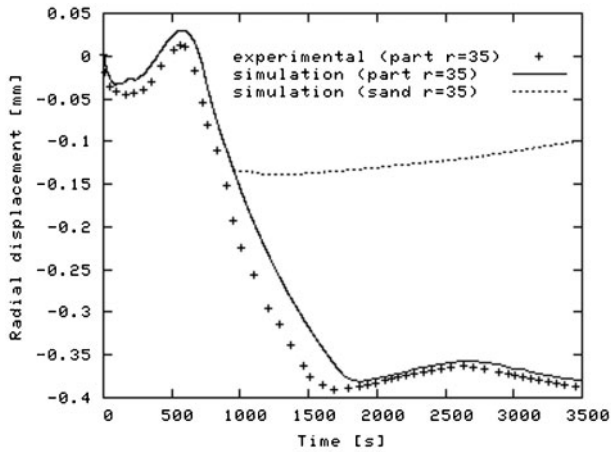
Density/ kg m^{-3} : 7900

Specific heat/ $\text{J kg}^{-1} \text{ }^{\circ}\text{C}^{-1}$: 490

Conductivity/ $\text{W m}^{-1} \text{ }^{\circ}\text{C}^{-1}$: 35

Table 4 Thermal properties of interfaces¹⁷

Interface	Temperature/ $^{\circ}\text{C}$	Heat transfer coefficient/ $\text{J s}^{-1} \text{ m}^{-2} \text{ }^{\circ}\text{C}^{-1}$
Casting/sand	20	500
	1170	1000
	1400	1000
Sand/steel		2000
Steel/air		20



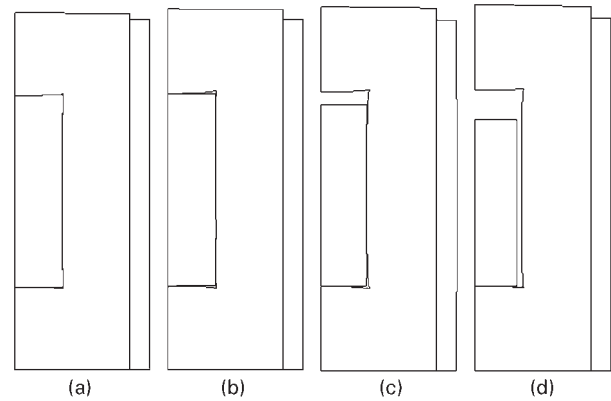
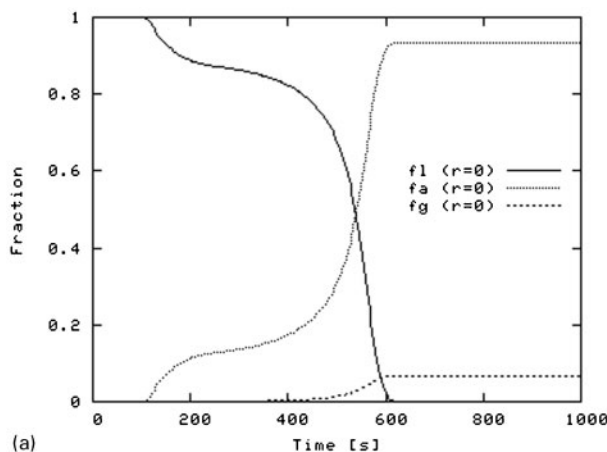
4 Experimental and computed radial displacement evolutions at height 85 mm of casting/sand interface

austenite and graphite volumetric fractions respectively). As in the experiments, it is seen that the final graphite content is nearly independent of the temperature rate (the final austenite and graphite volumetric fractions are found to be now more properly predicted than in Ref. 17 where the austenite fraction was underestimated in ~10%).

Figure 7 shows a comparison between the average experimental and computed final graphite nodule density distribution in the casting for two different radial positions at height 105 mm of the specimen where five families of nodules were defined to this end. It is seen that the model properly captures the fact that larger densities for the smaller nodules are expected in region with higher cooling rates. The model results also exhibit that the development of larger nodules is only possible in regions with low cooling rates. Although the computed predictions slightly overestimates the number of smaller nuclei, the numerical results are for the whole nodules size range in good agreement with the experimental observations (for family 1, the maximum standard deviation was 1×10^{13} nuclei mm^{-3}).

Conclusions

A large strain thermoplastic formulation for the analysis of the solidification process of SG cast irons of eutectic composition has been presented. This formulation



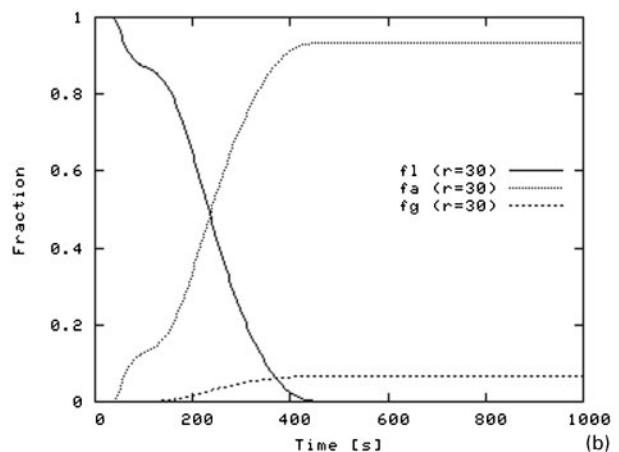
5 Computed deformed configurations at times a 200, b 500, c 1000 and d 3500 s (amplification factor=10)

accounts for thermomechanical as well as multinodular microstructure based behaviours of this material in a unified framework. Therefore, this feature allows the analysis of the different coupled and complex phenomena occurring in casting problems. Although the most important practical scope of this model is the possibility to control mechanical properties by predicting final graphite nodule size and distribution, the main limitations to its general application are related to the simplifying assumptions made in the thermomechanical behaviour of the mushy zone and in the austenite nucleation law.

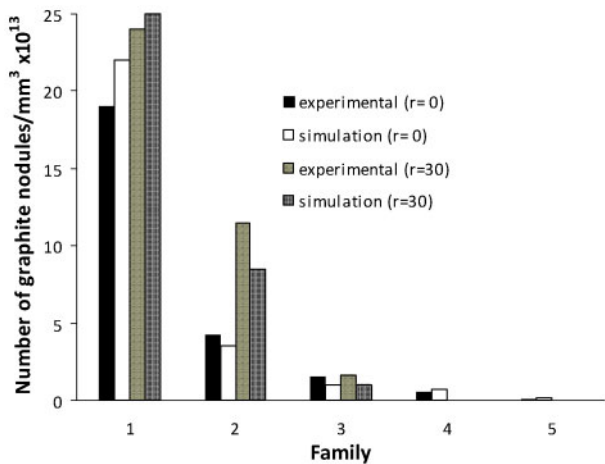
This formulation has been used in the analysis of a solidification test of SG cast iron in a green sand mould. The model has been partially validated with some available experimental measurements of temperature and displacement evolutions together with final values of austenite and graphite volumetric fractions and density of graphite nodules where reasonable agreements between numerical and experimental results can be observed. However, the difficulties associated to the full material characterisation lead to a further research in the thermomechanical–microstructural simulation of solidification processes with the sake of constituting a robust tool for casting design.

Acknowledgement

The support provided by CONICYT (FONDECYT project no. 1095195) is gratefully acknowledged.



6 Computed volumetric fractions evolutions in casting for radii a 0 and b 30 mm at height 105 mm of specimen



Family	Radius range [μm]
1	0 – 10
2	10 – 15
3	15 – 20
4	20 – 25
5	25 – 30

7 Experimental and computed final graphite nodule density distribution in casting for two different radial positions at height 105 mm of specimen

References

1. A. R. Kiani-Rashid and S. A. Rounaghi: 'The new methods of graphite nodules detection in ductile cast iron', *Mater. Manuf. Processes*, 2011, **26**, 242–248.
2. H. L. Zhao, M. F. Zhu and D. M. Stefanescu: 'Modeling of the divorced eutectic solidification of spheroidal graphite cast iron', *Key Eng. Mater.*, 2011, **457**, 324–329.
3. R. A. Gonzaga, P. Martínez Landa, A. Pérez and P. Villanueva: 'Mechanical properties dependency of the pearlite content of ductile irons', *J. Achiev. Mater. Manuf. Eng.*, 2009, **33**, (2), 150–158.2.
4. S. K. Putatunda: 'Comparison of the mechanical properties of austempered ductile cast iron (ADI) processed by conventional and step-down austempering process', *Mater. Manuf. Processes*, 2010, **25**, (8), 749–757.
5. Q. Ren, M. You, J. Yao, G. Wen and Q. Cai: 'Effect of yttrium-containing nodulizer on the microstructure formation and mechanical properties of heavy section ductile iron castings', *Key Eng. Mater.*, 2011, **457**, 73–78.
6. R. Gonzaga and J. Fernández Carrasquilla: 'Influence of an appropriate balance of the alloying elements on microstructure and on mechanical properties of nodular cast iron', *J. Mater. Process. Technol.*, 2005, **162–163**, 293–297.
7. M. Hatate, T. Shiota, N. Takahashi and K. Shimizu: 'Influences of graphite shapes on wear characteristics of austempered cast iron', *Wear*, 2001, **251**, 885–889.
8. P. Čanžar, Z. Tonković and J. Kodvanj: 'Microstructure influence on fatigue behaviour of nodular cast iron', *Mater. Sci. Eng. A*, 2012, **A556**, 88–99.
9. D. M. Stefanescu: 'Modeling of cast iron solidification – the defining moments', *Metall. Mater. Trans. A*, 2007, **38A**, 1433–1447.
10. H. Zhao and B. Liu: 'Modeling of stable and metastable eutectic transformation of spheroidal graphite iron casting', *ISIJ Int.*, 2001, **41**, (9), 986–991.
11. R. Boeri and A. Sikora: 'Solidification macrostructure of spheroidal graphite cast iron', *Cast Met. Res. J.*, 2001, **13**, 307–313.
12. P. Dardati, L. Godoy and D. Celentano: 'Microstructural simulation of solidification process of spheroidal-graphite cast iron', *ASME J. Appl. Mech.*, 2006, **73**, (6), 977–983.
13. D. J. Celentano, P. M. Dardati, L. A. Godoy and R. E. Boeri: 'Computational simulation of microstructure evolution during solidification of ductile cast iron', *Int. J. Cast Met. Res.*, 2008, **21**, (6), 416–426.
14. P. M. Dardati, D. J. Celentano, L. A. Godoy, A. A. Chiarella and B. J. Schulz: 'Analysis of ductile cast iron solidification: numerical simulation and experimental validation', *Int. J. Cast Met. Res.*, 2009, **22**, (5), 390–400.
15. A. Burelko, E. Fraš, D. Gurgul, W. Kapturkiewicz and J. Sikora: 'Simulation of the ductile iron solidification using a cellular automaton', *Key Eng. Mater.*, 2011, **457**, 330–336.
16. H. Zhao and B. Liu: 'Prediction of microstructure and porosity formation of practical spheroidal graphite iron castings', *Key Eng. Mater.*, 2011, **457**, 349–354.
17. D. Celentano: 'A large strain thermoviscoplastic formulation for the solidification of SG cast iron in a green sand mould', *Int. J. Plast.*, 2001, **17**, 1623–1658.
18. D. Celentano: 'Thermomechanical simulation and experimental validation of wire drawing processes', *Mater. Manuf. Processes*, 2010, **25**, (7), 546–556.
19. T. Midea and J. Shah: 'Mold material thermophysical data', *AFS Trans.*, 2002, **02-080**, 1–16.